BIOCHEMISTRY
including biophysical chemistry & molecular biology

Article

pubs.acs.org/biochemistry

Characterization of the Bacterioferritin/Bacterioferritin Associated Ferredoxin Protein−Protein Interaction in Solution and Determination of Binding Energy Hot Spots

Yan Wang,[†] Huili Yao,[†] Yuan Cheng,[‡] Scott Lovell,[§] Kevin P. Battaile,[∥] C. Russell Midaugh,[‡] and Mario Rivera*[,†]

[†]Department of Chemistry, University of Kansas, Multidisciplinary Research Building, 2030 Becker Drive, Room 220E, Lawrence, Kansas 66047, United States

[‡]Department of Pharmaceutical Chemistry, University of Kansas, Multidisciplinary Research Building, 2030 Becker Drive, Room 320G, Lawrence, Kansas 66047, United States

[§]Protein Structure Laboratory, Del Shankel Structural Biology Center, University of Kansas, 2034 Becker Drive, Lawrence, Kansas 66047, United States

[∥]IMCA-CAT, Hauptman Woodward Medical Research Institute, 9700 South Cass Avenue, Building 435A, Argonne, Illinois 60439, United States

Supporting Information

ABSTRACT: Mobilization of iron stored in the interior cavity of BfrB requires electron transfer from the [2Fe−2S] cluster in Bfd to the core iron in BfrB. A crystal structure of the *Pseudomonas aeruginosa* BfrB:Bfd complex revealed that BfrB can bind up to 12 Bfd molecules at 12 structurally identical binding sites, placing the [2Fe−2S] cluster of each Bfd immediately above a heme group in BfrB [Yao, H., et al. (2012) *J. Am. Chem. Soc., 134*, 13470−13481]. We report here a study aimed at characterizing the strength of the *P. aeruginosa* BfrB:Bfd association using surface plasmon resonance and isothermal titration calorimetry as well as determining the binding energy hot spots at the protein−protein interaction interface. The results show that the 12 Bfd-binding sites on BfrB are equivalent and independent and that the protein−protein association at each of these sites is driven entropically and is characterized by a dissociation constant (K_d) of approximately 3 μM. Determination of the binding energy hot spots was carried out by replacing certain residues that comprise the protein−protein interface with alanine and by evaluating the effect of the mutation on K_d and on the efficiency of core iron mobilization from BfrB. The results identified hot spot residues in both proteins [L_B^{68}, E_A^{81}, and E_A^{85} in BfrB (superscript for residue number and subscript for chain) and Y^2 and L^5 in Bfd] that network at the interface to produce a highly complementary hot region for the interaction. The hot spot residues are conserved in the amino acid sequences of Bfr and Bfd proteins from a number of Gram-negative pathogens, indicating that the BfrB:Bfd interaction is of widespread significance in bacterial iron metabolism.

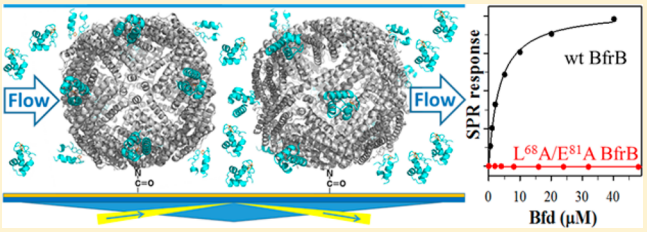

Iron is essential for bacteria due to its involvement in multiple metabolic processes including respiration (heme-containing proteins, [Fe−S]-containing ferredoxins) and key enzymatic reactions ([Fe−S]-containing proteins, such as fumarase and aconitase of the TCA cycle).[1] Pathogenic bacteria must obtain iron from the host to support growth, but humans maintain extremely low concentrations of free iron, which are further reduced during infections.[2,3] In bacterial cells, iron homeostasis plays a pivotal role in guarding against iron-induced toxicity caused by the propensity of free iron to stimulate the formation of reactive oxygen species (ROS) such as superoxide, hydrogen peroxide, and the highly destructive hydroxyl radical.[4] Consequently, free levels of iron in bacteria are tightly regulated to ensure sufficiency for metabolic needs while preventing iron-induced toxicity.[5] In humans, iron is stored in ferritin (Ftn),[6] whereas in bacteria, iron reserves are stored in a homologous bacterial Ftn and in bacterioferritin (Bfr), of which the latter is present only in bacteria.[7,8] Ftns, bacterial Ftns, and Bfrs assemble from 24 subunits into a hollow spherical structure with an outer diameter of 120 Å and an inner diameter of 80 Å, in which ≈3500 iron atoms can be stored in the form of an Fe^{3+} mineral. Despite their similar spherical architecture, eukaryotic and prokaryotic Ftns and Bfrs share <18% amino acid sequence homology. The unique primary sequence of each type of ferritin-like molecule strongly influences the packing of the corresponding 24-mer protein shells as well as their function.[9,10]

Received: August 20, 2015
Revised: September 11, 2015
Published: September 14, 2015

DOI: 10.1021/acs.biochem.5b00937
Biochemistry 2015, 54, 6162−6175

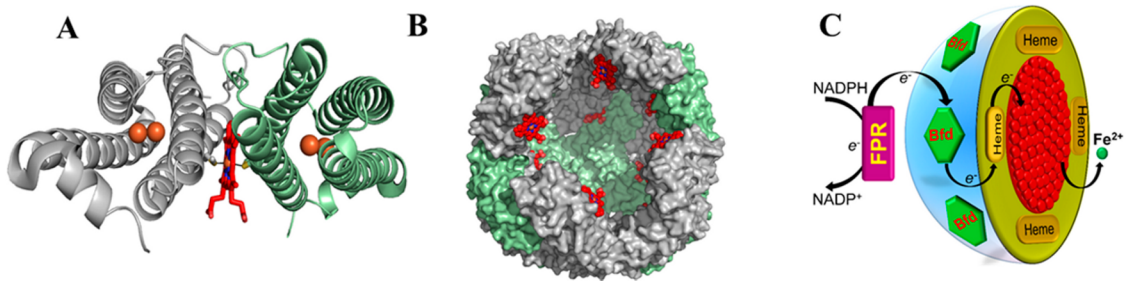

Figure 1. Structural organization of BfrB (PDB: 3IS8) and schematic representation of the process of iron mobilization from BfrB. (A) View of a subunit dimer harboring a heme molecule (red), which is coordinated by a conserved methionine from each of the subunits. (B) View of the BfrB interior cavity where iron mineral is stored; heme (red) is buried below the protein shell surface, with the heme propionates extending into the interior cavity. (C) Model of iron mobilization from the BfrB interior cavity, where electrons from NADPH are transferred via FPR and Bfd into the Fe^{3+} mineral stored in the core of BfrB.

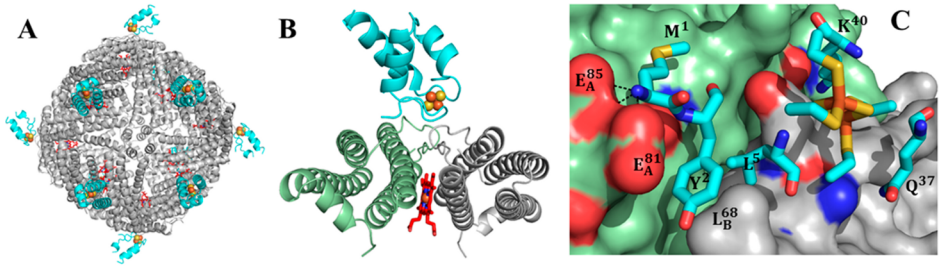

Figure 2. Structure of the BfrB:Bfd complex (PDB: 4E6K). (A) Twelve Bfd molecules bind a 24-mer BfrB at 12 identical binding sites. (B) Each Bfd molecule (cyan) binds at the interface of a BfrB subunit dimer, above a heme molecule. (C) Zoomed-in view of the BfrB:Bfd interface depicting residues in Bfd (cyan sticks) interacting with the BfrB surface; subunit A in BfrB is rendered green, and subunit B is gray. O, N, S, and Fe are shown in red, blue, yellow, and orange, respectively.

Bfrs are unique in possessing intrinsic heme groups, which are bound at 2-fold intersubunit sites by axial coordination of the heme-iron by methionine residues from adjacent subunits (Figure 1A). Hence, a 24-mer Bfr can be thought of as being assembled from 12 subunit dimers, each harboring a heme, which is buried deep below the protein surface, such that the heme propionates reach into the interior cavity (Figure 1B).[7] Bfrs function by (i) utilizing O_2 or H_2O_2 to oxidize Fe^{2+} and store Fe^{3+} in their internal cavity (core) and (ii) accepting electrons to reduce Fe^{3+} in their core and mobilize Fe^{2+} to the cytosol.[11,12] In bacteria, the concentration of iron not incorporated in proteins (free iron), Fe^{2+}, is maintained by a dynamic equilibrium between Fe^{3+} stored in ferritin-like molecules and Fe^{2+}. Hence, one function of ferritin-like molecules is to maintain the cytosolic Fe^{2+} concentrations that enable Fur, the major iron-responsive regulator which is conserved in many bacteria,[13] to perform its broad range of regulatory functions that link iron homeostasis to broader bacterial metabolism.[14−16] For example, Bfr mutants of *Mycobacterium tuberculosis* suffer from iron-mediated oxidative stress and are unable to persist in mice and guinea pig models of infection.[17,18] A Bfr-deficient mutant of *Nisseria gonorrheae* is growth-impaired in iron-limited medium and more sensitive to killing by hydrogen peroxide,[19] and in the plant pathogen *Erwinia chrysanthemi*, mutation of the *bfr* gene results in impaired iron utilization and growth defects.[20]

Early studies with *Escherichia coli* suggested that mobilization of iron from Bfr requires interactions with a ferredoxin, dubbed Bfd (bacterioferritin-associated ferredoxin) because the *bfd* gene is adjacent to the *bfr* gene.[21−23] While mining the global genetic response of *Pseudomonas aeruginosa* to high and low iron conditions,[24] we noticed that of the ≈120 genes reported to be upregulated by low-iron conditions, the expression of *bfd* is upregulated 200-fold and that of a gene coding for a ferredoxin reductase (*fpr*) is increased 3-fold.[24] In contrast, the *bfrB* gene is downregulated under iron-limiting conditions.[25] The strong upregulation of the *bfd* gene in response to low iron led us to hypothesize that the Bfd protein functions in the mobilization of iron stored in BfrB by accepting electrons from the ferredoxin reductase (FPR) and transferring these to the ferric iron in BfrB for subsequent mobilization of Fe^{2+} (Figure 1C).[26] We cloned the genes, characterized the *P. aeruginosa* BfrB, Bfd, and FPR proteins biochemically and structurally,[27,28] and showed that Bfd, FPR, and NADPH are sufficient to mobilize iron from BfrB *in vitro*.[26]

More recently, we reported the X-ray crystal structure of the BfrB:Bfd complex.[12] The asymmetric unit contains three BfrB subunit dimers, each associated with a Bfd molecule, giving rise to a biological assembly consisting of a nearly spherical 24-mer BfrB with 12 Bfd molecules (Figure 2A). Each Bfd binds at an identical site on BfrB, at the interface of a subunit dimer, above each of the heme molecules, placing the [2Fe−2S] cluster of Bfd approximately 22 Å from the heme-iron in BfrB (Figure 2B). Studies in solution demonstrated that formation of the BfrB:Bfd complex enables the heme in BfrB to conduct electrons from the [2Fe−2S] cluster in Bfd to the mineral core, thus accelerating reduction of the Fe^{3+} mineral core and the mobilization of Fe^{2+}.[12,26] A zoomed-in view of one of the 12 identical Bfd-binding sites on BfrB (Figure 2C) illustrates the proximity of the [2Fe−2S] cluster to the BfrB surface and shows the interactions that are likely important to stabilize the complex: (i) The side chain of Y^2 in Bfd anchors in a cleft on the BfrB surface, which is formed by the side chains of E^{81} in subunit A (E_A^{81}) and L^{68} in subunit B (L_B^{68}), (ii) the side chain of L^5 in Bfd fits in a pocket formed mostly by L_B^{68}, N_B^{70}, L_B^{71}, and L_A^{77}, (iii) the backbone NH

DOI: 10.1021/acs.biochem.5b00937
Biochemistry 2015, 54, 6162−6175

group of M^1 forms H-bonds with carboxyl side chains in E_A^{85} and E_A^{81} on BfrB and its side chain interacts hydrophobically with L_A^{77}, L_A^{78}, I_A^{79}, G_A^{80}, and C_A^{89} on the BfrB surface, and (iv) the side chain of K^{40} in Bfd interacts hydrophobically with the side chain of K_A^{76} in BfrB and forms hydrogen bonds with carbonyl oxygen of BfrB Q_B^{72} and L_A^{74}.

In the present study, we examined the BfrB:Bfd interaction in solution with the aid of surface plasmon resonance (SPR) and isothermal titration calorimetry (ITC) and determined that the 12 Bfd-binding sites on BfrB, which are structurally identical, are also independent. Bfd binds at each of the sites on BfrB with a K_d of approximately 3 μM, and the interaction, although endothermic, is favored by a relatively large change in entropy. Having obtained a benchmark for the interaction between the two proteins, we mutated several residues that comprise the interface to alanine. These experiments revealed how particular side chains and the Bfd binding surface of BfrB contribute to the stability of the complex and to the Bfd-promoted mobilization of core iron from BfrB. While conducting this work, we noticed that recombinant BfrB used in our prior studies contained an extra methionine at position zero (M^0), immediately upstream from the initiator methionine. We used site-directed mutagenesis to eliminate M^0 and demonstrated that M^0 BfrB is structurally identical to wt BfrB and that M^0 BfrB binds Bfd with a K_d indistinguishable from the K_d obtained for the association between Bfd and wt BfrB.

EXPERIMENTAL PROCEDURES

Site-Directed Mutagenesis. Mutations were introduced to the recombinant *bfd* and *bfrB* genes[26] with the aid of the Quik Change mutagenesis kit (Stratagene, La Jolla, CA) using the manufacturer's instructions. Primer pair sequences are provided in Supporting Information. Mutations were confirmed by sequencing (ACGT Inc., Wheeling, IL). The $C^{43}S$ mutant of Bfd is more stable to purification and manipulation but has the same functional and spectroscopic properties as those of wt Bfd; just as important, C43 is not a ligand to the [2Fe−2S] cluster, and it is far from the area used by Bfd to bind BfrB.[12,26] Consequently, the $C^{43}S$ mutant will be referred to as wt Bfd in this article. The following mutations were introduced to the wt *bfd* gene: Y^2A, Y^2F, L^5A, and $K^{40}A$. The extra methionine (M^0) in recombinant BfrB was removed by eliminating the corresponding codon in the *bfrB* gene. BfrB with the correct sequence is termed wt BfrB, and BfrB harboring the extra methionine will be referred to as M^0 BfrB.

Protein Expression and Purification. Recombinant FPR and Bfd (wt and mutants) were expressed and purified as described previously.[28] Recombinant BfrB (wt and all mutants) were expressed and purified using previously reported protocols[12,26] with some modifications: *E. coli* Arctic express RIL cells harboring the recombinant pET11a/*bfrB* construct were cultured overnight at 37 °C in 50 mL of LB medium containing 100 μg/mL ampicillin and 20 μg/mL gentamicin. The cells were then cultured in 1 L of fresh LB containing no antibiotics for 3 h at 30 °C, transferred to a shaker incubator pre-equilibrated at 10 °C, and incubated for 45 min before protein expression was induced by addition of 1 mM 1-thio-D-galactopyranoside (IPTG). Cells were cultured for an additional 48 h at 10 °C before they were harvested by centrifugation and stored at −20 °C. Cell paste was suspended in a solution containing 50 mM Tris-Base (pH 7.6), 5 mM dithiothreitol (DTT), 0.5 mM phenylmethanesulfonylfluoride (PMSF), and 0.5% Triton X-100 (Sigma) and sonicated on ice. Cell debris were pelleted by centrifugation at 4 °C and 19 500 rpm, and the supernatant was dialyzed against 50 mM Tris-Base (pH 7.6), loaded onto a Q-Sepharose Fast Flow column (12 cm × 2.5 cm i.d.) equilibrated with the same buffer, and eluted with a gradient of 0 to 600 mM NaCl. Fractions containing BfrB were dialyzed against 50 mM potassium phosphate buffer (pH 7.6) containing 1 mM tris(2-carboxyethyl)phosphine (TCEP), loaded onto a hydroxyapatite Bio-Gel column (10 cm × 2.5 cm i.d.) equilibrated with the same buffer, and eluted with a 50 to 800 mM potassium phosphate gradient (pH 7.6), 1 mM TCEP. Isolating fractions containing BfrB and repeating this chromatographic step yield pure BfrB. The separation of 24-mers from incompletely assembled protein was carried out by FPLC (AKTA GE Healthcare) in a Hiload 16/600 superdex 200 pg column equilibrated and eluted with 100 mM potassium phosphate (pH 7.0). BfrB purified in this manner is nearly devoid of heme. To reconstitute with heme, a previously described method[29] was used with some modifications: Hemin chloride was dissolved in 0.1 M sodium hydroxide solution and diluted with potassium phosphate buffer (100 mM, pH 7.0) to a final concentration of 1.5 mM. Insoluble material was removed by centrifugation. BfrB (3 μM) in 100 mM potassium phosphate (pH 7.0) and 1 M NaCl was equilibrated at 80 °C for 1 min in a dry bath (LabDoctor Dry Bath Plus), followed by the addition of a first aliquot of heme, which delivered 6 heme molecules per 24-mer BfrB, and the mixture was incubated for 10 min at 80 °C. The temperature was then increased to 90 °C prior to addition of a second aliquot of heme delivering 6 heme molecules per 24-mer BfrB, followed by incubation at 90 °C for 10 min. The temperature was then increased to 95 °C prior to addition of a third aliquot of heme delivering 6 heme molecules per 24-mer, followed by incubation of the mixture at 95 °C for 10 min. The resultant mixture was cooled on ice and loaded onto a Hiload 16/600 Superdex 200 pg column equilibrated and eluted with 100 mM potassium phosphate (pH 7.6) at 4 °C. The desired fractions were collected and supplemented with 1 mM TCEP. The heme content of BfrB was analyzed according to a previously described method.[26,30] Reconstitution of BfrB with an iron core was carried out as reported previously.[26] Upon addition of 500 Fe ions/BfrB, the protein solutions were incubated overnight at 4 °C and then passed through a Superdex 200 10/300 GL column. The content of iron in bacterioferritin, before and after reconstitution with an iron core, was measured using a previously reported protocol.[26,31]

Crystallization and X-ray Diffraction Data Collection. Crystallization experiments were conducted in Compact 300 sitting drop vapor diffusion plates (Rigaku Reagents) at 20 °C. Equal volumes of BfrB (10 mg/mL in 100 mM potassium phosphate, pH 7.6 and 1 mM TCEP) and crystallization solution were mixed and equilibrated against 75 μL of crystallization solution. All crystals were obtained from the Wizard 3-4 screen (Rigaku Reagents) except for the wt BfrB crystals, which employed the Cryo HT screen (Rigaku Reagents). All crystals were observed within 1 to 2 days. The observed morphology, crystallization conditions, and cryoprotectants are as follows. wt BfrB: Crystals displaying plate morphology were obtained in 1 to 2 days from condition H6 (30% (v/v) PEG 200, 100 mM Na acetate, pH 4.5, 200 mM sodium chloride). Crystals were transferred to a fresh drop of crystallant, which served as the cryoprotectant. $L^{68}A$ BfrB: Prismatic crystals from well E10 (50% (v/v) PEG 200, 100 mM Na cacodylate, pH 6.5, 200 mM magnesium chloride) were transferred to a drop of crystallant, which served as the cryoprotectant. $L^{68}A/E^{81}A$ BfrB: Prismatic

DOI: 10.1021/acs.biochem.5b00937
Biochemistry 2015, 54, 6162−6175

crystals from well A2 (30% (v/v) 2-methyl-2,4-pentanediol, 100 mM Na acetate, pH 4.6, 20 mM calcium chloride) were transferred to a fresh drop of crystallant, which served as the cryoprotectant. $E^{81}A$ BfrB: Plate shaped crystals from well F12 (2.4 M sodium malonate) were transferred to a drop of 3.4 M sodium malonate, which served as the cryoprotectant. $E^{85}A$ BfrB: Plate shaped crystals from well F4 (15% (v/v) PEG 550MME, 100 mM MES, pH 6.5) were transferred to a drop containing 25% PEG 550MME and 75% crystallant. Fe-soaked crystals of wt and $L^{68}A/E^{81}A$ BfrB were prepared by soaking native crystals for 10 min in 50 mM $FeCl_2$ freshly dissolved in crystallization solution and frozen in liquid nitrogen. X-ray diffraction data were collected at the Advanced Photon Source Beamline 17-ID (Argonne National Laboratory) using a Dectris Pilatus 6 M pixel array detector. All diffraction data sets were collected at λ = 1.0000 Å except for the iron-bound crystals, which were collected at λ = 1.720 Å in order to obtain the maximum iron anomalous signal. The anomalous difference maps were used to assign iron atoms to specific sites, and peak heights and *B*-factors of the iron atoms were compared for each particular structure.

Structure Solution and Refinement. Intensities were integrated using XDS,[32] and the Laue class analysis and data scaling were performed with Aimless.[33] Structure solution was conducted by molecular replacement with Phaser[34] using a single subunit of a previously determined BfrB structure (PDB: 3IS7) as the search model. Refinement and manual model building were conducted with Phenix[35] and Coot,[36] respectively. Structure validation was conducted with Molprobity.[37] Disordered side chain atoms were truncated to the point where electron density could be observed. Further details are provided below, and relevant crystallographic data are provided in Table S1 of the Supporting Information.

$L^{68}A$ BfrB. The highest probability Laue class was *mmm*, and the suggested space group was $P2_12_12_1$, with a = 117.86 Å, b = 125.66 Å, and c = 169.99 Å. On the basis of the Matthew's coefficient[38] (V_m = 2.9 Å^3/Da, 58% solvent), the asymmetric unit likely contained 12 molecules of BfrB. The top solution was obtained in the space group $P2_122_1$, with 12 molecules in the asymmetric unit. Since $P2_122_1$ is a nonstandard setting of $P2_12_12$, the data were reindexed using the operator $(h,-l,k)$ to transform the reflections into the standard space group setting $P2_12_12$ with a = 117.86 Å, b = 169.99 Å, and c = 125.66 Å

Following initial refinement, large peaks of electron density were observed in the 4-fold pores and B-pores. The 4-fold pores of BfrB are typically occupied by K^+ ions.[27] However, large peaks of positive electron density ($F_o - F_c$) greater than 3σ were observed at these sites when modeled as K^+ ions. A phased anomalous difference map revealed peaks at the K^+ binding sites of the 4-fold pore that were between 10σ and 11σ. Given that the crystals were obtained from cacodylate buffer and the maximum anomalous signal for arsenic is at approximately λ = 1.047 Å (f″ ∼ 3.9e^-), it appeared that arsenic ions of some form occupied the 4-fold pore sites. The data for this structure were collected at λ = 1.0000 Å, which would still yield an appreciable anomalous signal (f″∼ 3.6e^-). It was clear from the electron density, however, that a cacodylate ion was not bound to this region and thus the electron density was ultimately modeled as AsH_3 (Figure S1). It is unclear how this form of arsenic would be bound at this site, but perhaps it is due to impurities in the cacodylate buffer or due to reactivity with the TCEP that is present in the protein storage buffer. The B-pores also displayed large peaks of electron density, which were modeled as Mg^{2+} ions obtained from the crystallant. Most of the Mg^{2+} are hexacoordinated by water molecules, which also form contacts with residues in the B-pores (Figure S2).

$L^{68}A/E^{81}A$ BfrB. The highest probability Laue class was −3, and the suggested space groups were $P3$, $P3_1$, or $P3_2$. On the basis of the Matthew's coefficient[38] (V_m = 2.9 Å^3/Da, 57% solvent), the asymmetric unit likely contained 24 molecules of BfrB. All space groups with 3 point symmetry were tested, and the top solution was obtained in space group $P3_2$ with 24 molecules in the asymmetric unit.

$E^{81}A$ BfrB. The highest probability Laue class was *mmm*, with possible space groups $C222$ or $C222_1$. On the basis of the Matthew's coefficient[38] (V_m = 2.9 Å^3/Da, 55% solvent), the asymmetric unit likely contained 12 molecules of BfrB. The top solution was obtained in space group $C222_1$.

$E^{85}A$ BfrB. The highest probability Laue class was 4/*mmm*, with the highest probability space group being $P4_22_12$. On the basis of the Matthew's coefficient[38] (V_m = 2.8 Å^3/Da, 56% solvent), the asymmetric unit likely contained 12 molecules of BfrB. All space groups with 422 point symmetry were tested, and the top solution (12 molecules/ASU) was obtained in space group $P4_22_12$.

Measurement of the BfrB:Bfd Binding Affinity by Surface Plasmon Resonance (SPR). SPR experiments were performed at 22 °C using a Biacore 3000 instrument (GE Healthcare). BfrB was immobilized on a CM5 sensor chip using amine coupling chemistry.[39] The sensor chip surface was preconditioned with 50 mM NaOH, 10 mM HCl, 0.1% SDS, and 0.085% H_3PO_4 and activated by injecting 0.1 M *N*-hydroxysuccinimide (NHS) and 0.4 M 1-ethyl-3-(3-(dimethylamino)propyl) carbodiimide (EDC) in water. The running buffer was PBS with 1.5 mM TCEP, pH 7.4. Immobilization of BfrB was carried out by flowing (10 μL/min) a 100 nM solution of BfrB in 10 mM sodium acetate buffer (pH 5.0) for 32.5 min, followed by quenching surface-activated sites not coupled to BfrB by flowing (10 μL/min) 1.0 M aqueous ethanolamine-HCl (pH 8.5) for 7 min. A cell activated by NHS/EDC and quenched by ethanolamine but not containing BfrB was used as the reference surface, and a cell immobilized with bovine serum albumin (BSA) was used as control. To determine the BfrB:Bfd binding affinity, a solution of Bfd in 50 mM potassium phosphate (pH 7.0), 150 mM NaCl, 5 mM DTT was simultaneously flowed (25 μL/min) over the cell containing immobilized BfrB, the reference cell, and the cell containing immobilized BSA at 25 μL/min. Bfd solutions with the following concentrations were used to construct a binding curve: 0.5, 1.0, 2.0, 5.0, 10.0, 20.0, and 40.0 μM. The corresponding responses were double-referenced by subtracting the bulk refractive index change caused by difference in buffer compositions as well as by subtracting the response from the reference cell. Experiments were conducted in triplicate.

Measurement of the BfrB:Bfd Binding Affinity by Isothermal Titration Calorimetry (ITC). Prior to each experiment, BfrB and Bfd were exchanged into 100 mM potassium phosphate buffer (pH 7.0), 150 mM NaCl, and 1 mM TCEP by passage through a Superdex 200 10/300 GL or superdex 75 10/300 GL column, respectively. ITC was performed at 22 °C using a MicroCal auto ITC instrument (GE Healthcare). The cell was loaded with 1.45 mL of 18 μM Bfd and titrated with a total volume of 0.25 mL of 20 μM BfrB in 25 injections, each lasting 20 s and delivering 10.02 μL, with 300 s between injections. A similar titration of BfrB into buffer served as a control to measure the heat of dilution. The experiment was repeated three times.

DOI: 10.1021/acs.biochem.5b00937
Biochemistry 2015, 54, 6162−6175

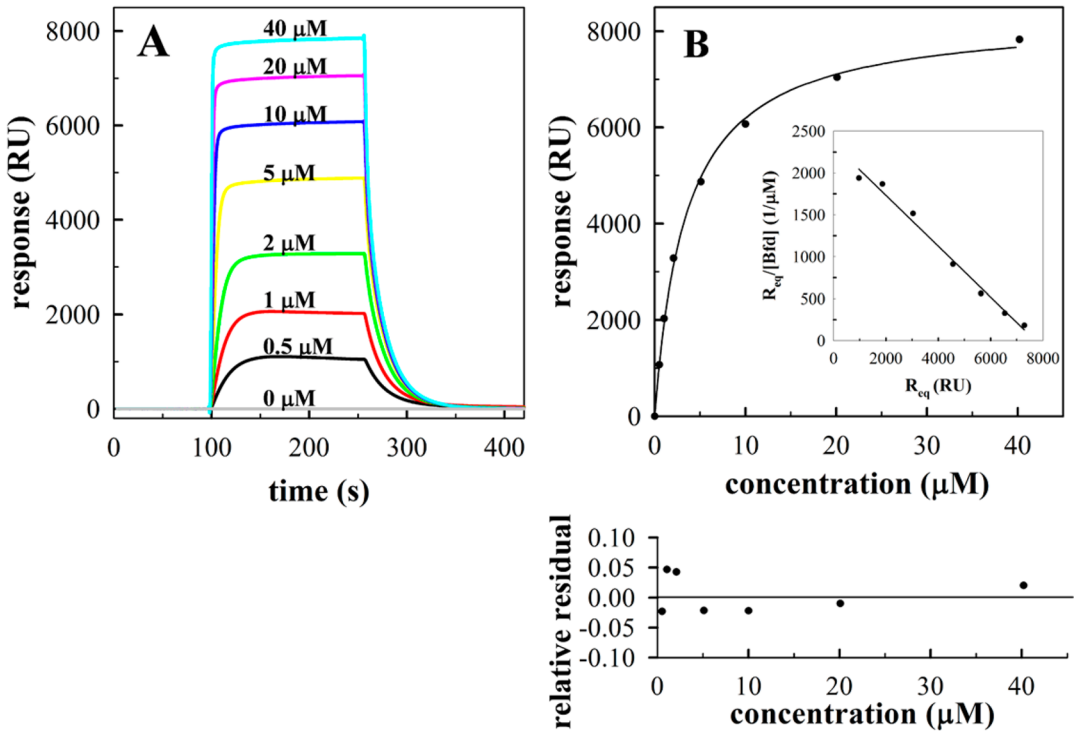

Figure 3. Measuring the affinity of the BfrB:Bfd interaction using SPR. (A) Overlay of reference- and baseline-subtracted sensograms resulting from flowing wt Bfd solution of the indicated concentration over immobilized wt BfrB. (B) BfrB:Bfd binding affinity determined by steady-state affinity analysis. Responses at steady state are plotted as a function of Bfd concentration (black circles in top panel) and fitted to the model described by eq 4 (solid line). The bottom panel shows the relative differences between the fitted and experimental data. A Scatchard plot is shown in the inset of the top panel.

Mobilization of Iron from BfrB. These experiments were carried out in an anaerobic chamber according to a previously described method[26] with small modifications: A 1 cm path-length cuvette was filled with a solution consisting of BfrB (0.18 μM) reconstituted with 500 ± 20 Fe^{3+} ions/BfrB, Bfd (0.9 μM), FPR (7.2 μM), and α,α'-bipyridine (bipy), 3 mM. The reactions leading to mobilization of Fe^{2+} from BfrB (Figure 1C) were initiated by addition of 1 mM NADPH, and the process was monitored by tracking the time-dependent formation of the $[Fe(bipy)_3]^{2+}$ complex, which absorbs at 523 nm. The percentage of iron released was calculated by normalizing the intensity of the 523 nm band to the intensity expected upon mobilization of the 500 iron ions stored in BfrB.

RESULTS AND DISCUSSION

Characterization of the BfrB:Bfd Interaction by SPR Shows That the 12 Bfd-Binding Sites on BfrB Are Identical and Independent. The X-ray crystal structure of the BfrB:Bfd complex showed that each Bfd binds at the interface of a BfrB subunit, near the 2-fold axis of symmetry, placing the [2Fe−2S] cluster of Bfd approximately 22 Å from the heme-iron in BfrB.[12] Studies in solution showed that Bfd binding to BfrB makes the BfrB-heme conductive, accelerates reduction of the Fe^{3+} mineral core, and facilitates mobilization of Fe^{2+}.[7,26] As part of this study, we investigated the binding affinity of the BfrB:Bfd complex using SPR. Figure 3A shows the reference- and baseline-subtracted responses obtained from flowing wt Bfd over wt BfrB immobilized on a sensor chip. At each Bfd concentration, the corresponding response reaches a plateau, indicating steady-state equilibrium. Plotting each response at steady state as a function of Bfd concentration results in the hyperbolic binding curve defined by the black circles in Figure 3B. The interpretive model used to fit these data is described below.

In the SPR experiments, BfrB was immobilized on the surface and free Bfd was in the flow. Hence, $[BfrB_f]$ is the concentration of immobilized BfrB not bound to Bfd, $[Bfd_f]$ is the concentration of Bfd in the flowing solution, which is maintained constant by the flow system, and [BfrB:Bfd] is the concentration of the protein complex at the surface. For a case where Bfd binding is homogeneous and the stoichiometry is 1:1, the expression for the dissociation constant (K_d) can be written as in eq 1,[40] where the total concentration of immobiled BfrB is given by $[BfrB_t] = [BfrB_f] + [BfrB:Bfd]$.

$$\frac{[BfrB:Bfd]}{[BfrB_t]} = \frac{[Bfd_f]}{K_d + [Bfd_f]} \quad (1)$$

Since the X-ray crystal structure showed that Bfd binds to multiple sites on BfrB, eq 1 was modified to eq 2, which indicates that n sites in BfrB can be occupied by Bfd, with corresponding dissociation constants.

$$[BfrB:Bfd] = [BfrB:Bfd_1] + [BfrB:Bfd_2] + \ldots + [BfrB:Bfd_n] = \frac{[BfrB_t][Bfd_f]}{K_{d1} + [Bfd_f]} + \frac{[BfrB_t][Bfd_f]}{K_{d2} + [Bfd_f]} + \ldots + \frac{[BfrB_t][Bfd_f]}{K_{dn} + [Bfd_f]} \quad (2)$$

The X-ray crystal structure of the BfrB:Bfd complex also showed that the Bfd molecules bind at 12 structurally identical binding sites on BfrB. Thus, assuming that the 12 Bfd binding sites on BfrB are identical and noninteracting, eq 2 can be reduced to eq 3,[40] which is similar to eq 1, except for the inclusion of the complex stoichiometry, n.

DOI: 10.1021/acs.biochem.5b00937
Biochemistry 2015, 54, 6162−6175

Table 1. Thermodynamic and Kinetic Parameters for the BfrB:Bfd Interaction[a]

	K_d (μM)	k_a (μM^{-1} s^{-1})	k_d (s^{-1})	ΔH (kcal/mol)	ΔS (cal/(mol K))[b]	ΔG (kcal/mol)[c]
SPR equilibrium analysis	3.3 ± 0.5[d]					
SPR kinetic analysis	2.6 ± 0.4[d]	0.026 ± 0.002	0.069 ± 0.01			
ITC analysis	4.2 ± 0.4[e]			1.6 ± 0.3	30.1 ± 0.7	−7.3 ± 0.1

[a]The reported thermodynamic and kinetic parameters obtained from triplicate experiments at 22 °C. [b]Calculated from $\Delta G = \Delta H - T\Delta S$ [c]Calculated from $\Delta G = -RT \ln(1/K_d)$ [d]K_d obtained at pH 7.4 [e]K_d obtained at pH 7.0

$$[\text{BfrB:Bfd}] = \frac{n[\text{BfrB}_t][\text{Bfd}_f]}{K_d + [\text{Bfd}_f]} \quad (3)$$

At each of the Bfd concentrations ($[\text{Bfd}_f]$) used in the SPR experiments shown in Figure 3A, when the system reaches steady-state equilibrium (at the plateau), the concentration of the BfrB:Bfd complex at the surface is proportional to the magnitude of the SPR response at the pleateau, which is termed R_{eq}. Hence, eq 3 can be rewritten as eq 4, where R_0, corresponds to the response when every immobilized 24-mer BfrB molecule is bound by one Bfd molecule, and the remainder terms are defined as above. The value of R_0 can be estimated from eq 5,[41] where R_{immo} is the SPR response obtained upon immobilizing BfrB, MW_{BfrB} is the molecular mass of BfrB (452 672 Da), and MW_{Bfd} is the molecular mass of Bfd (7984 Da).

$$R_{eq} = \frac{nR_0[\text{Bfd}_f]}{K_d + [\text{Bfd}_f]} \quad (4)$$

$$R_0 = \frac{MW_{Bfd}}{MW_{BfrB}} \times R_{immo} \quad (5)$$

Setting initial values of $n = 12$ and $R_0 = 520$, respectively, and fitting the values of R_{eq} obtained from each $[\text{Bfd}_f]$ (circles in the plot of Figure 3B) to eq 4, values for $K_d = 3.3 \pm 0.5$ μM (Table 1), $n = 12.7$, and $R_0 = 624 \pm 18$ were obtained. As can be seen from the fitted line in Figure 3B and from the small relative residuals, the binding curve is well-fitted by eq 4. In addition, the linear behavior observed from analysis of the binding curve by the Scatchard plot, which is a powerful tool for identifying deviations from simple binding models,[40] supports the idea implicit in eq 4, namely, that the 12 binding sites in BfrB are equivalent and independent.

Having shown that the 12 binding sites on a BfrB molecule are identical and independent, kinetic analysis of the BfrB:Bfd interaction was carried out assuming the 1:1 binding model described by eqs 6 and 7, where BfrB_s indicates one of the 12 binding sites in each immobilized BfrB molecule, $[\text{BfrB}_{ts}]$ is the total concentration of binding sites (12/BfrB molecule) on the surface, $[\text{BfrB}_{bs}]$ is the concenration of BfrB sites bound to Bfd, k_a is the association rate constant, and k_d is the dissociation rate constant. Equation 7 can be rewritten in terms of the SPR response as eq 8, where R is the response caused by Bfd binding and R_{max} is the response when all the binding sites are occupied by Bfd.[42] Hence, values of k_a and k_d (Table 1) were obtained from global fitting of the SPR data to eq 8 (Figure 4) with the aid of BIAevaluation software. Note that the ratio of the constants ($k_a/k_d = 2.6$ μM) is very similar to the value of K_d obtained from steady-state analysis described above, an observation that strengthens the conclusion that the Bfd binding sites on BfrB are independent and equivalent.

$$\text{BfrB}_s + \text{Bfd} \underset{k_{off}}{\overset{k_{on}}{\rightleftarrows}} \text{BfrB}_s\text{:Bfd} \quad (6)$$

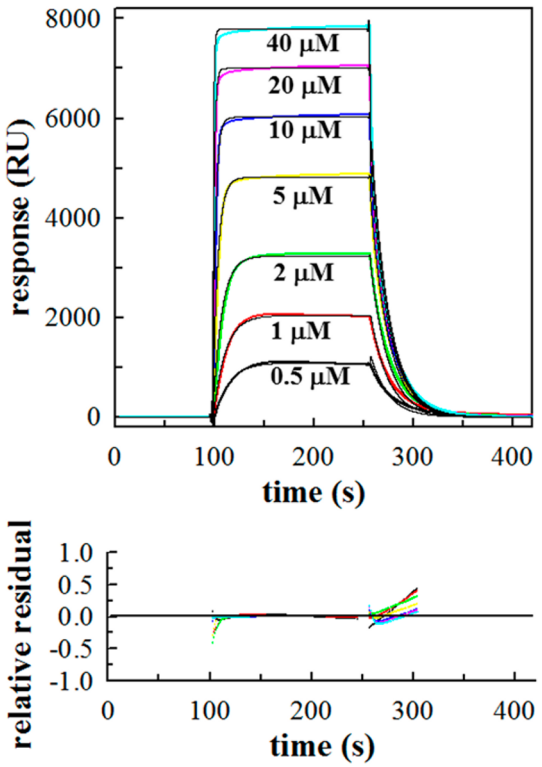

Figure 4. Kinetic analysis of the BfrB:Bfd interaction. Top: Reference- and baseline-subtracted sensograms obtained from flowing wt Bfd solution of the indicated concentration over immobilized wt BfrB shown in different colors. Corresponding fitted traces are shown in black. Relative residuals are shown in the bottom panel.

$$\frac{d[\text{BfrB}_{bs}]}{dt} = k_a([\text{BfrB}_{ts}] - [\text{BfrB}_{bs}])[\text{Bfd}_f] - k_d[\text{BfrB}_{bs}] \quad (7)$$

$$\frac{dR}{dt} = k_a(R_{max} - R)[\text{Bfd}_f] - k_dR \quad (8)$$

Characterization of the BfrB:Bfd Interaction by ITC. The interaction between wt BfrB and wt Bfd was also studied by ITC at 22 °C. The top panel in Figure 5, which shows the binding isotherms obtained from titrating Bfd with BfrB, indicates that formation of the BfrB:Bfd complex is an endothermic process. The ITC data were integrated, normalized for nonspecific heat effects, and fitted using a nonlinear least-squares algorithm (minimization of χ^2) with the aid of the Origin software package provided by MicroCal. Since the 12 binding sites on BfrB are equivalent and independent, the data were fitted to the 1:1 binding model described by eq 6, where the concentration of titrant (BfrB) is the concentration of Bfd-binding sites (subunit dimers). Fitting the integrated heats (bottom panel in Figure 5) allowed us to obtain the ΔH, ΔS, and K_d values listed in Table 1, which indicate that the BfrB:Bfd association is entropically

DOI: 10.1021/acs.biochem.5b00937
Biochemistry 2015, 54, 6162−6175

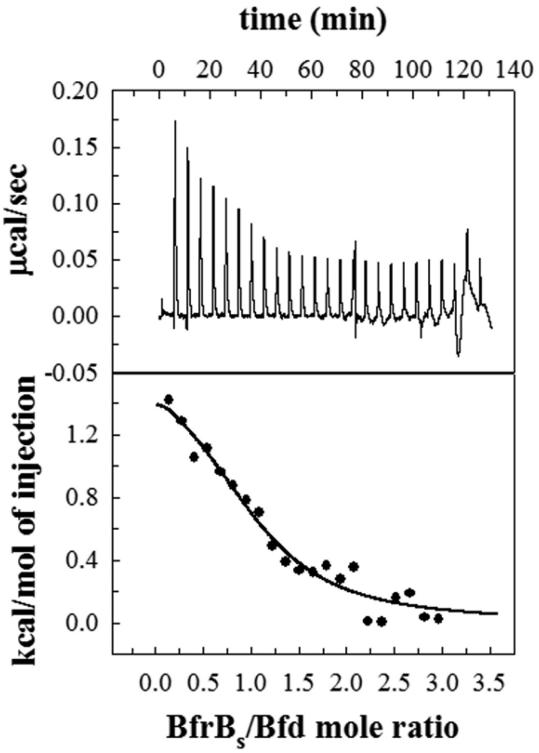

Figure 5. Analysis of the BfrB:Bfd interaction using ITC. Top: Heat absorbed upon titrating BfrB into Bfd. Bottom: Integrated heats plotted against the BfrB$_s$/Bfd mole ratio and fitted to the 1:1 binding model described by eq 6.

driven. Note that the value of K_d obtained from these measurements is in good agreement with the K_d value obtained from the SPR experiments, thus providing additional support for the idea that the 12 Bfd-binding sites in BfrB are identical and independent. Identical experiments (SPR and ITC) were carried out with M^0 BfrB (Figures S3 and S4). The results show that the K_d values obtained by SPR (K_d = 3.8 ± 0.2 μM) and ITC (K_d = 2.6 ± 1.0 μM) are within error, indistinguishable from those obtained with wt BfrB. Hence, the M^0 residue has no influence on the BfrB:Bfd association. Moreover, as will be shown below, M^0 has no influence on the BfrB structure.

Dissecting the Interaction Surface in the BfrB:Bfd Complex. The structure of the BfrB:Bfd complex shows that L^{68}, E^{81}, and E^{85} in BfrB interact with M^1, Y^2, and L^5 in Bfd (see Figure 2C), forming a contiguous set of interactions that is likely to contribute significantly to the stability of the complex. To study the relative contribution of these interactions to the formation of the complex, we prepared the L^{68}A, E^{81}A, E^{85}A, L^{68}A/E^{81}A mutants of BfrB and the Y^2A, Y^2F, L^5A, and K^{40}A mutants of Bfd. It has been shown that in BfrB breathing motions of the protein shell link relatively remote sections in the structure and that, for example, mutations in some of the pores can affect the reactivity of relatively distant ferroxidase centers.[9] The main objective of the mutations introduced in wt BfrB for this study is to determine their effect on the stability of the BfrB:Bfd interaction and concomitant inhibition of mobilization of iron stored in the BfrB core. Consequently, we characterized the BfrB mutants to determine that the site-directed mutations, which were designed to affect only the BfrB:Bfd interaction, did not cause significant changes in the structure of the protein or its ability to oxidize Fe^{2+} and store Fe^{3+}. The biochemical characterization is described immediately below, and the structural analysis is presented later, after we have discussed the functional implications.

Biochemical and Functional Characterization of BfrB Mutants. The ability of the mutant proteins to assemble into 24-mers was analyzed with the aid of a calibrated size exclusion column. The results show that retention volumes exhibited by all of the mutants are nearly identical to the retention volume displayed by wt BfrB (Figure S5), indicating that all mutants assemble into 24-mers. Additionally, the UV−vis absorption spectrum displayed by each of the BfrB mutants is identical to that of wt BfrB and M^0 BfrB (Figure S6): The heme in the oxidized form gives rise to a Soret band at 418 nm, whereas in its reduced form, the Soret band is at 425 nm with peaks in the visible at 527 and 567 nm. In wt BfrB, the ratio A_{280}/A_{418} = 0.67 is indicative of a 24-mer protein harboring 12 heme molecules.[26] In the UV−vis spectra obtained from each of the BfrB mutants, the A_{280}/A_{418} ratio is also ≈0.67, indicating that the mutants also harbor 12 hemes in a 24-mer assembly. This conclusion is also supported by analysis of heme content.

The Fe^{2+} oxidation and Fe^{3+} uptake function of each mutant were evaluated by reconstituting each of the proteins with 500 iron ions and monitoring the process by UV−vis spectrophotometry, as described previously.[26,27] The spectral data (Figure S7) obtained from titrating a solution of BfrB with aliquots delivering 50 Fe^{2+} ions/BfrB show a gradual increase in the absorption at 300 nm, which is associated with the growth of a Fe^{3+} mineral in the core of ferritin-like molecules.[26] After addition of 500 Fe ions/BfrB, the solution was incubated overnight at 4 °C and then passed through a Sephadex G-25 column. Subsequent determination of iron content in BfrB showed that each of the proteins captured >450 Fe^{3+} ions/BfrB. Having determined that the BfrB mutants assemble into fully functional 24-mers capable of oxidizing Fe^{2+} and storing Fe^{3+} in their core, the effect of the mutations on the ability of Bfd to bind BfrB mutants and promote the mobilization of core iron was examined.

Mobilization of Core Iron from the BfrB Mutants Is Compromised. We have previously demonstrated that mobilization of Fe^{3+} stored in BfrB requires Bfd[12,26] and that the process of iron mobilization (shown schematically in Figure 1C) involves Bfd binding to BfrB, which permits electron transfer from the [2Fe−2S] cluster in Bfd to the core Fe^{3+} mineral in BfrB via its heme. Consequently, to determine the effect of the BfrB mutations on the ability of Bfd to bind and promote the mobilization of core Fe^{3+}, we reconstituted wt and each of the BfrB mutants with 500 ± 20 Fe^{3+} ions in their core (Figure S7). Mobilization of the iron core was monitored by UV−vis spectrophotometry, where the reaction mixture contained wt, BfrB, FPR, Bfd, and an excess of bipyridine (bipy), a Fe^{2+} chelator. Addition of excess NADPH initiates the reactions shown in Figure 1C, and the release of Fe^{2+} from BfrB is monitored by ΔA_{523}, which tracks the time-dependent formation of the $[Fe(bipy)_3]^{2+}$ complex. The black circles in Figure 6A track ΔA_{523} normalized to the total absorbance change expected upon removal of the 500 iron ions from wt BfrB core. In comparison, the reaction carried out in the absence of Bfd (red circles, Figure 6A) clearly demonstrates that there is no formation of $[Fe(bipy)_3]^{2+}$ and, consequently, no mobilization of BfrB from the iron core. Thus, Bfd is necessary for the efficient and quantitative mobilization of Fe^{2+} from BfrB.

Similar experiments conducted with the BfrB mutants show that the mutations significantly decrease the efficiency of iron mobilization: Replacement of Leu^{68}, Glu^{81}, or Glu^{85} for Ala

DOI: 10.1021/acs.biochem.5b00937
Biochemistry 2015, 54, 6162−6175

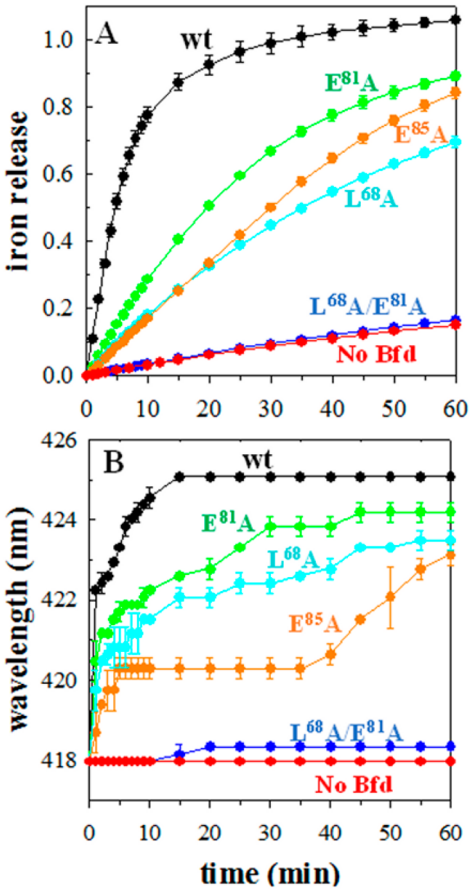

Figure 6. Mobilization of Fe^{3+} stored in mutant BfrBs designed to block the BfrB:Bfd interaction is impaired. (A) Time-dependent increase in the normalized ΔA_{523} upon addition of excess NADPH (final concentration, 1.0 mM) to 20 mM phosphate buffer (pH 7.6) containing 0.9 μM wt Bfd, 7.2 μM Fpr, and 0.18 μM of wt (black), $E^{81}A$ (green), $L^{68}A$ (cyan), $E^{85}A$ (orange), $L^{68}A/E^{81}A$ BfrB (blue) or no BfrB (red). (B) Time-dependent changes in the position of the heme Soret band in BfrB on addition of NADPH to the solutions in panel A; 418 and 425 nm correspond to fully oxidized and fully reduced heme, respectively.

causes significant decrease in the rate of iron release from BfrB, as shown by the cyan, green, and orange traces in Figure 6A. It is noteworthy that iron release from the $Leu^{68}Ala/Glu^{81}Ala$ double mutant is nearly completely abolished, as shown by the blue trace. To facilitate a more quantitative comparison of the effect of the mutations on the rates of iron mobilization, the initial rates of iron mobilization were obtained from fitting the initial, linear part of the curves (0 to ~4 min) to a linear function (Table 2).

The accompanying plots in Figure 6B track the time-dependent shift of the Soret band from 418 nm (oxidized heme) to 425 nm (reduced heme). In the case of wt BfrB, as the iron mobilization process progresses and the Fe^{3+} mineral core has been ≈80% mobilized, the heme is completely reduced, indicating that when the iron core is significantly diminished the flux of electron transfer from Bfd to heme in BfrB is faster than the flux of electron transfer from the heme to the Fe^{3+} core. When $L^{68}A$, $E^{81}A$, or $E^{85}A$ are utilized, reduced heme accumulates more gradually, and the corresponding ferric cores are mobilized more slowly than that in wt BfrB. In the case of the $E^{81}A/L^{68}A$ BfrB mutant, the Fe^{3+} core is not mobilized (Figure 6A), and the heme remains oxidized (Soret band remains at 418 nm). These observations are consistent with the idea that the interaction between $L^{68}A/E^{81}A$ BfrB and Bfd is blocked, which inhibits electron transfer and Fe^{3+} mobilization. Taken together, the observations summarized in Figure 6 indicate that Bfd and BfrB single mutants undergo interactions conducive to electron transfer less frequently than Bfd and wt BfrB and that interactions between $L^{68}A/E^{81}A$ BfrB and Bfd, if they occur at all, are not conducive to electron transfer.

Table 2. Dissociation Constants for the BfrB:Bfd Interaction Involving Mutant BfrB and Bfd Molecules and Corresponding Initial Rates of Iron Release from the Core of BfrB

protein	K_d (μM) (pH 7.4)	initial rate (min^{-1})
wild type	3.3 ± 0.5	0.099 ± 0.007
BfrB E81A	258.5 ± 21.5	0.031 ± 0.0003
BfrB L68A	298.5 ± 20.5	0.019 ± 0.0003
BfrB E85A	590 ± 2	0.018 ± 0.0006
BfrB L68A/E81A	not measurable	not measurable
Bfd Y2F	10.7 ± 0.2	0.097 ± 0.004
Bfd K40A	7.7 ± 0.5	0.090 ± 0.002
Bfd L5A	82 ± 2.5	0.044 ± 0.0005

The BfrB Mutants Have Significantly Reduced Affinity for Bfd. The findings described in the section above suggest that, relative to wt BfrB, the BfrB mutants form less stable complexes with Bfd. Experimental support for this idea was obtained by measuring the K_d for the associations between Bfd and each of the BfrB mutants using SPR, in a manner similar to that described above for the association between wt BfrB and Bfd. Figure 7A–D illustrates the reference- and baseline-subtracted responses obtained from flowing Bfd over immobilized $L^{68}A$, $E^{81}A$, $E^{85}A$, and $L^{68}A/E^{81}A$ BfrB, respectively. For each of the mutants, the corresponding response reaches a plateau at each of the Bfd concentrations, indicating steady-state equilibrium. Plotting each response at steady state as a function of Bfd concentration produces the binding plots defined by the black ($E^{81}A$), red ($L^{68}A$), and green ($E^{85}A$) circles in Figure 7E. Fitting the data to eq 4 produced the corresponding K_d values, which are listed in Table 2. The data shows that the association between Bfd and $L^{68}A$ or $E^{81}A$ BfrB is ≈100 times weaker than the corresponding association with wt BfrB and that the $E^{85}A$ mutation results in the lowest affinity for Bfd, which is ≈170 times lower than that measured for wt BfrB. Note that the reference- and baseline-subtracted responses obtained from flowing Bfd over immobilized $L^{68}A/E^{81}A$ BfrB (Figure 7D) indicate that the association between these two proteins is undetectable by SPR. The affinity of Bfd for BfrB decreases in the order wt ≫ $E^{81}A$ ≈ $L^{68}A$ > $E^{85}A$ ≫ $L^{68}A/E^{81}A$ (Table 2), which suggests that the efficiency of core iron mobilization might follow a similar order. The pseudo rate constants of iron mobilization, however, follow the order wt ≫ $E^{81}A$ > $L^{68}A$ ≈ $E^{85}A$ ≫ $L^{68}A/E^{81}A$. The explanation for these seeming discrepancies probably resides in the fact that binding affinity is not the only determinant for electron transfer between the two proteins. Rather, interactions conducive to electron transfer must place the [2Fe–2S] cluster of Bfd in relative close (optimum) proximity to the heme in BfrB so that electron transfer is facilitated. Consequently, although the binding affinity of $L^{68}A$ > $E^{85}A$, it is possible that $E^{85}A$ interacts with Bfd in a manner conducive to electron transfer more frequently than does the $L^{68}A$ mutant.

Structural Characterization of BfrB Mutants. The X-ray crystal structure of wt BfrB is nearly identical to the previously reported structure of M^0 BfrB (PDB 3IS7); superposition[43] of subunit A of wt BfrB with subunit A of M^0 BfrB resulted in 0.20 Å

DOI: 10.1021/acs.biochem.5b00937
Biochemistry 2015, 54, 6162–6175

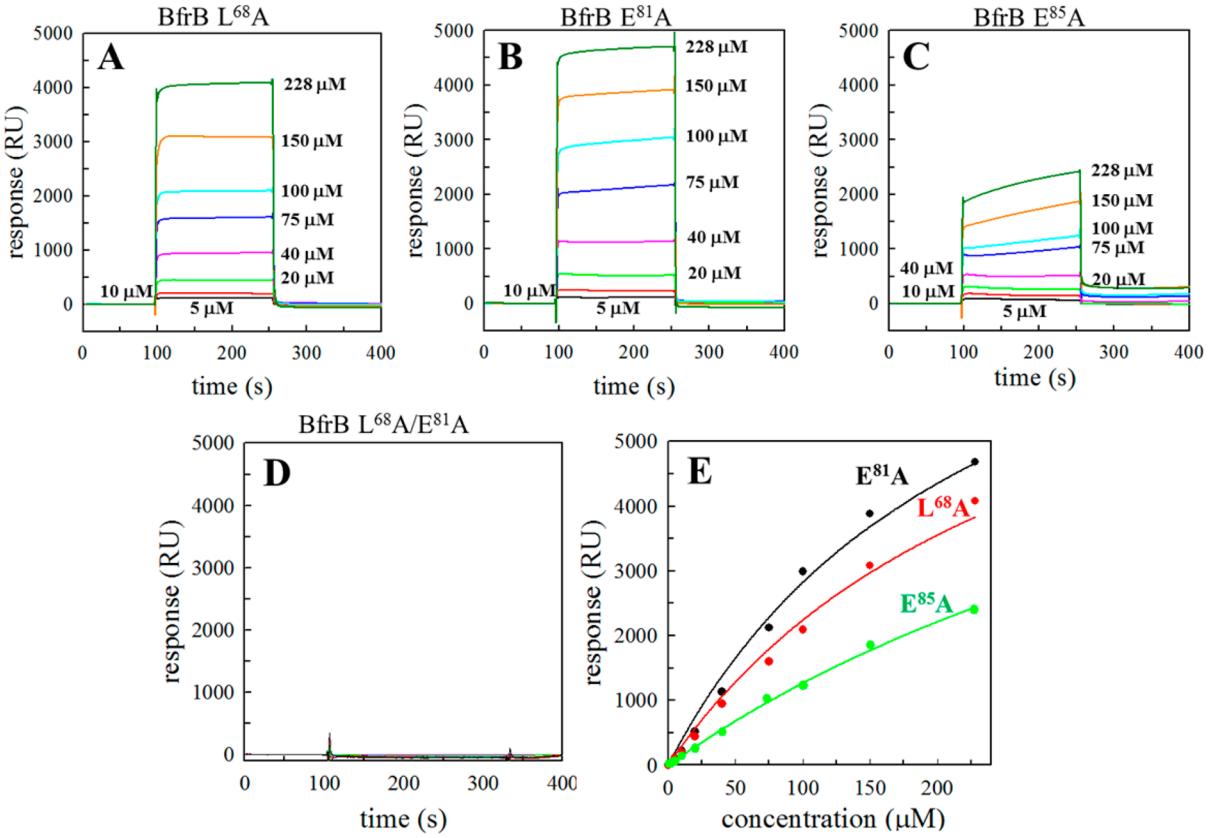

Figure 7. Binding affinity of Bfd for mutant BfrBs is diminished. Overlay of reference- and baseline-subtracted sensograms resulting from flowing wt Bfd at the indicated concentrations over immobilized (A) $L^{68}A$, (B) $E^{81}A$, (C) $E^{85}A$, and (D) $L^{68}A/E^{81}A$ BfrB. (E) Responses at steady state were plotted as a function of Bfd concentration and fitted to the model described by eq 4.

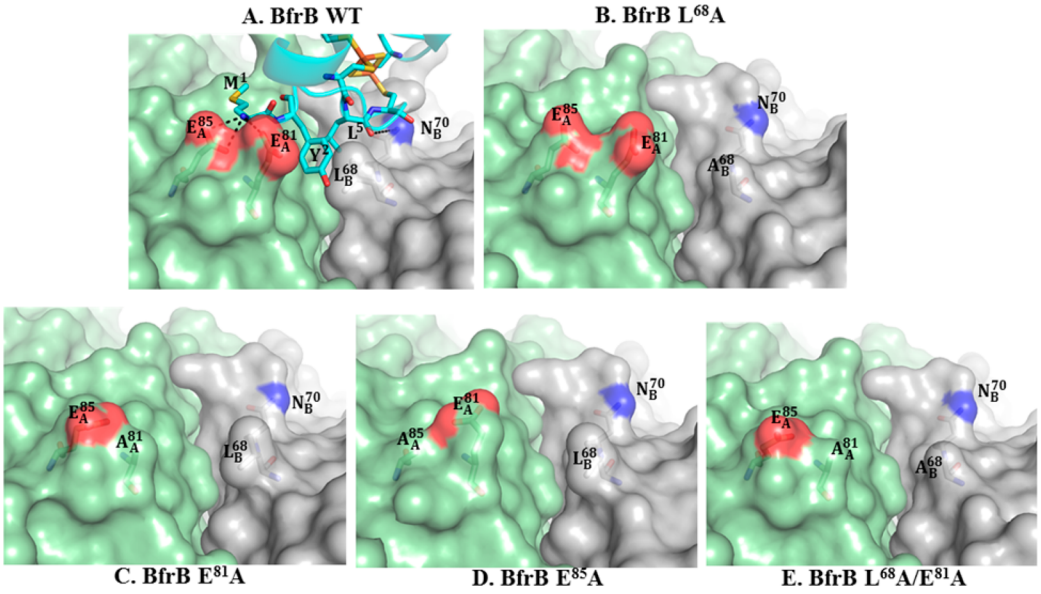

Figure 8. Structural changes in the Bfd-binding sites of BfrB mutants. (A) View of the wt BfrB:Bfd interface, showing Bfd residues in cyan sticks and BfrB in surface representation, with subunit A in green and subunit B in gray. (B–E) Identical views of the Bfd-binding sites in the BfrB mutants, illustrating the structural changes in each of the BfrB mutants. O and N atoms are in red, and S and Fe atoms in the [2Fe–2S] cluster of Bfd are in yellow and orange, respectively.

RMSD between C_α atoms for the 153 residues aligned using secondary structure matching.[44] Superposition of the wt BfrB structure with the structures of each of the BfrB mutants in this study shows that the overall organization of the mutants is nearly identical to that of the wt protein. The RMSD values (C_α atoms) obtained from superposing subunit A of wt BfrB with subunit A of $L^{68}A$, $E^{81}A$, $E^{85}A$, and $L^{68}A/E^{81}A$ BfrB are 0.19, 0.25, 0.22, and 0.15 Å, respectively, for 156 residues aligned. Our previous work showed that in all structures of as-isolated M^0 BfrB the ferroxidase centers are devoid of iron. Soaking crystals of as-

DOI: 10.1021/acs.biochem.5b00937
Biochemistry 2015, 54, 6162–6175

isolated protein in crystallization solution containing $FeCl_2$, however, invariably resulted in iron binding at the ferroxidase centers. We also noted that iron binding is always accompanied by a conformation change of the ferroxidase center ligand H^{130} side chain from a gate-open to gate-closed state.[9,27] Hence, it is not surprising that in this study soaking crystals of wt and mutant BfrBs in $FeCl_2$ solution resulted in iron binding to the ferroxidase centers and in conformation change of the H^{130} side chain from gate open to gate closed (Figure S8). Interestingly, the ferroxidase iron ions in wt and $L^{68}A/E^{81}A$ BfrB are also bridged by an acetate ion obtained from the crystallization buffer. These observations, which indicate that the ferroxidase centers in the mutant BfrB molecules are functional *in crystallo*, are in good agreement with ferroxidase center competency in solution, as demonstrated in the above-described Fe^{2+} oxidation and Fe^{3+} uptake efficiency in solution (Figure S7). Consequently, it is clear that the mutations do not affect the iron oxidation function or the global structure of BfrB. As will be shown below, small structural changes observed in each of the BfrB mutants near the mutated residue are consistent with their lower binding affinity for Bfd.

The structure of the BfrB:Bfd complex showed that Bfd binding to BfrB is accompanied by relatively small rearrangements on the BfrB surface.[12] The most significant rearrangements are the reorientation of the $L^{68}A$, $E^{81}A$, and $E^{85}A$ side chains on BfrB, which enable hydrophobic and hydrophilic interactions with Bfd: rearrangement of the L^{68} and E^{81} side chains narrows the cleft formed by the two side chains, which serves as a pocket to receive the Y^2 side chain from Bfd (Figure 8A). The new conformation of the L^{68} side chain also contributes to the narrowing of the pocket where the L^5 side chain from Bfd anchors on the BfrB surface. The side chain reorientations of E^{81} and E^{85} enable H-bonding interactions between the backbone carbonyl oxygen of Y^2 in Bfd and the carboxylic group of E^{81}, as well as the backbone N−H of M^1 in Bfd and the carboxylic group in E^{81} and E^{85}. These interactions, in turn, allow the side chain of M^1 in Bfd to pack hydrophobically against the BfrB surface. Close inspection of the Bfd-binding site in $L^{68}A$ BfrB (Figure 8B) shows that the conformation of the E^{81} side chain remains as in the wt protein but that the shorter side chain of A^{68} makes the cleft shallower on one side. This is expected to affect the extent to which the Bfd Y^2 side chain can bind and also affect the pocket where Bfd L^5 anchors on the BfrB surface. The structure of the $E^{81}A$ mutant (Figure 8C) suggests that, in addition to a shallower more open cleft where the anchoring of Y^2 from Bfd is likely to be less efficient, a hydrogen bond between the NH of M^1 in Bfd and a carboxyl O in BfrB E^{81} is lost. The shorter A^{85} side chain in the $E^{85}A$ mutant (Figure 8D) allows the E^{81} side chain to move away from the cleft and therefore create a wider gap, which is probably unfavorable for efficient anchoring of the Bfd Y^2 side chain. In addition, the hydrogen bonds between NH of M^1 in Bfd and the carboxyl oxygens in BfrB E^{85} are no longer possible, which, in turn, may have an unfavorable effect on how the side chain of M^1 in Bfd packs against the BfrB surface. In aggregate, the $E^{85}A$ mutation eliminates more interactions than the $L^{68}A$ or $E^{81}A$ mutation, which is in agreement with the observation that the K_d measured for the interaction between Bfd and $E^{85}A$ BfrB is approximately 2-fold larger than the K_d values measured for the complexes formed between Bfd and $L^{68}A$ BfrB or $E^{81}A$ BfrB (Table 2). Finally, the structure of the $L^{68}A/E^{81}A$ mutant (Figure 8E) shows a very wide cleft, where the Y^2 side chain in Bfd is unlikely to undergo any meaningful interactions. This is probably the reason that the association between Bfd and the BfrB double mutant is blocked and mobilization of core iron stored in $L^{68}A/E^{81}A$ BfrB is inhibited.

Mutations in Bfd. The X-ray crystal structure of the BfrB:Bfd complex revealed, for the first time, the Bfd fold, which consists of a helix-turn-helix motif, where the four Cys ligands to iron in the [2Fe−2S] cluster are located in two hairpin loops (Figure 9). Note that iron ligands C^4 and C^6 are located in the same hairpin loop (cyan) that contains M^1, Y^2, and L^5, whose side chains anchor Bfd at the BfrB surface. We prepared the Y^2A, Y^2F, L^5A, and $K^{40}A$ Bfd mutants to evaluate the effect of the mutations on the association with BfrB and their effectiveness at promoting the mobilization of core iron from BfrB. The L^5A and $K^{40}A$ mutants can be expressed and purified in yields comparable to those of wt Bfd. The mutants display UV−vis spectra nearly identical to that of the wt protein (Figure S9), indicating that they bind a [2Fe−2S] cluster. In contrast, Y^2A Bfd is expressed in the *E. coli* host cells but does not incorporate a [2Fe−2S] cluster. Inspection of the wt Bfd structure shows that the Y^2 side chain contributes to stabilizing the hairpin loop containing C^4 and C^6 via packing interactions with G^8 and T^{10} (Figure 9). It is therefore possible that the inability of the Y^2A mutant to bind a [2Fe−2S] cluster is a consequence of conformational disorder in the loop containing iron ligands C^4 and C^6. Given that Y^2A Bfd cannot bind a [2Fe−2S] cluster, we prepared the Y^2F mutant in an attempt to study the role played by the phenolic OH in BfrB:Bfd association and in promoting the mobilization of core iron from BfrB.

The dissociation constant for the interaction between BfrB and each of the mutant Bfds was measured using SPR. The corresponding reference- and baseline-subtracted sensograms (Figures 10A and S10) show that each of the systems attains steady-state equilibrium, so K_d values (Table 2) were obtained from fitting the corresponding data to eq 4 (Figure 10B). The K_d obtained with Y^2F Bfd is approximately 3 times larger than that measured with wt Bfd, which indicates that the phenol OH in Y^2 contributes only modestly to stabilizing the BfrB:Bfd complex. This observation is consistent with our analysis of the interface, which shows that anchoring of the Y^2 side chain engages mainly hydrophobic interactions with L^{68} and E^{81} in BfrB (Figure 2C). The K_d measured with L^5A Bfd, on the other hand, is ≈30-fold higher than that obtained with wt Bfd, a finding that is also

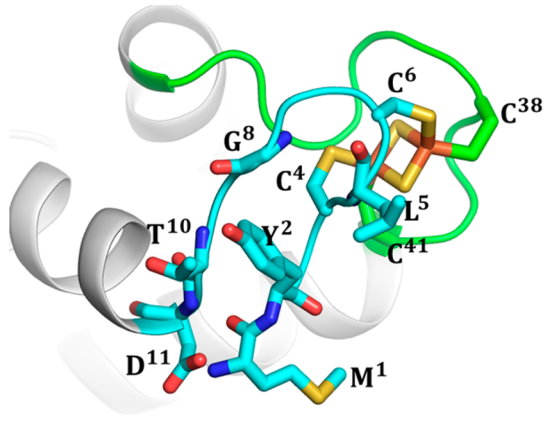

Figure 9. Structural organization of the hairpin loops harboring the iron ligands in the [2Fe−2S] cluster of Bfd (PDB 4E6K). The N′-terminus hairpin loop (cyan) contains residues Y^2 and L^5 and iron ligands C^4 and C^6; packing interactions involving Y^2, G^8, and T^{10} stabilize the hairpin and the [2Fe−2S] cluster. The hairpin loop containing iron ligands C^{38} and C^{41} is shown in green; O, N, S, and Fe atoms are shown in red, blue, yellow, and orange, respectively.

DOI: 10.1021/acs.biochem.5b00937
Biochemistry 2015, 54, 6162−6175

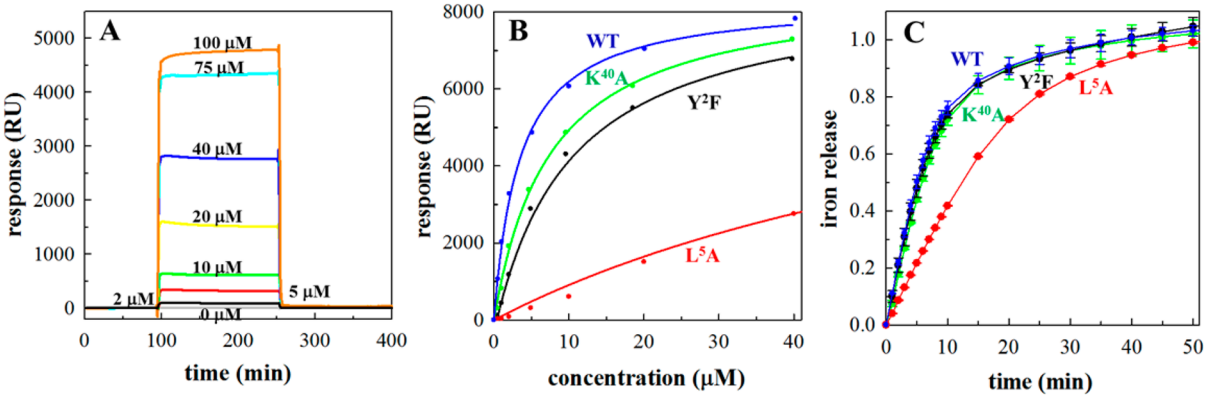

Figure 10. Effect of mutations in Bfd on the binding affinity of the BfrB:Bfd complex and on iron mobilization from wt BfrB. (A) Overlay of reference- and baseline-subtracted sensograms resulting from flowing L^5A Bfd solution of the indicated concentrations over immobilized wt BfrB. (B) Responses at steady state plotted as a function of the concentration of wt (blue), L^5A (red), Y^2F (black), and $K^{40}A$ Bfd (green). (C) Time-dependent increase in the normalized ΔA_{523} upon addition of excess NADPH (final concentration, 1.0 mM) to 20 mM phosphate buffer (pH 7.6) containing 0.18 μM wt BfrB, 7.2 μM Fpr, and 0.9 μM wt (blue), Y^2F (black), L^5A (red), or $K^{40}A$ Bfd (green).

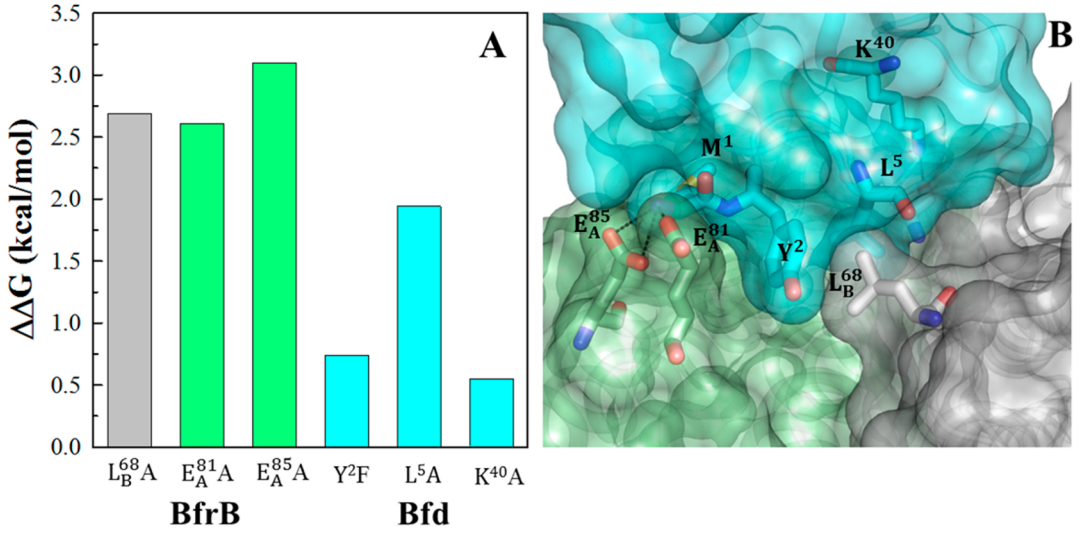

Figure 11. Identification of hot spot residues at the interface of the BfrB:Bfd complex. (A) Change in binding free energy ($\Delta\Delta G$) brought by mutations in BfrB (green for subunit A; gray for subunit B) or in Bfd (cyan). (B) Zoomed-in view of the BfrB:Bfd interface depicting how hot spot residues network into a hot region; O is in red, and N is in blue.

consistent with our analysis of the interface, which suggests that packing of the L^5 side chain on the BfrB surface is important for the stabilization of the BfrB:Bfd complex. The K_d obtained with $K^{40}A$ Bfd is 2 times larger than the K_d obtained with wt BfrB. Analysis of the interface shows that the hydrophobic portion of the K^{40} side chain interacts with the hydrophobic portion of BfrB K_A^{76}; in addition, K^{40} forms hydrogen bonds with Q_B^{72} and L_A^{74} in BfrB. Although it is possible that the A^{40} side chain in K40A Bfd partially substitutes for the hydrophobic stabilization provided by the K^{40} and BfrB K_A^{76} packing interaction, the modest increase in K_d observed with the $K^{40}A$ mutant suggests that K^{40} is less important to the stabilization of the BfrB:Bfd complex than Y^2 and L^5. The relative stability of the complexes formed between BfrB and mutant Bfds (wt $\approx$ Y^2F $\approx$ $K^{40}A$ > L^5A) is reflected in the ability of each of these mutants to promote the mobilization of core iron from BfrB (Figure 10C and Table 2). It is interesting to note that under the conditions of our iron mobilization assay an increase in K_d of approximately 3 times does not significantly affect the efficiency of iron mobilization. This may be due to the presence of a large excess of NADPH in the cuvette.

Concluding Remarks. In this study, we have dissected the BfrB:Bfd interface to validate the model obtained from the X-ray crystal structure and to gain a greater understanding of the interactions that contribute to the stability of this protein−protein complex. The results, which demonstrate that replacing key residues at the protein−protein interface for alanine lowers the strength of the association and impairs core iron mobilization, are in excellent agreement with the structural model, which places the [2Fe−2S] cluster in Bfd immediately above the heme in BfrB to facilitate electron transfer. Our findings also provide significant insight into factors that contribute to the stability of the BfrB:Bfd complex. In this context, it is important to note that although the number of structures of protein−protein complexes is relatively limited, analysis of protein−protein complexes has shown that not all residues participating at protein−protein interfaces contribute equally to the stability of the complex. Rather, there are critical residues that contribute to the majority of the binding energy. Thus, these have been termed hot spot residues. Hot spot residues can be identified by alanine-scanning mutagenesis, if

DOI: 10.1021/acs.biochem.5b00937
Biochemistry 2015, 54, 6162−6175

their substitution by alanine leads to a binding energy difference of at least 2 kcal/mol ($\Delta\Delta G \geq 2$ kcal/mol).[45−47] Hot spot residues tend to occur in clusters, which often form a network of interactions constituting hot regions; importantly, such a hot region includes residues from both proteins.[48] Our results, which show that replacing L_B^{68}, E_A^{81}, and E_A^{85} in BfrB and L^5 in Bfd for alanine results in $\Delta\Delta G \geq 2$ kcal/mol, clearly identify these as hot spot residues (Figure 11A). A zoomed-in view of the BfrB:Bfd interface (Figure 11B) illustrates how these critical residues form a clustered network of packing interactions that define a hot region. The figure also makes it evident that Y^2 in Bfd is probably an integral component of the hot region. As pointed out above, the Y^2A Bfd mutant cannot bind a [2Fe−2S] cluster and therefore could not be studied. Nevertheless, the structure suggests that hydrophobic packing of its aromatic side chain with the L_B^{68} side chain and the hydrophobic portion of the E_A^{81} side chain in BfrB dominate the contribution of Y^2 to the stability of the complex. Identification of the hot spot residues in both proteins, as well as visualization of the hot region, makes it apparent that a large portion of the hot spot interactions is eliminated from the hot region by replacing E_A^{81} and E_A^{85} in BfrB for alanine, which should significantly decrease the binding affinity, a prediction that is reflected in the observation that Bfd cannot bind to L^{68}A/E^{81}A BfrB. Finally, it is noteworthy that all of the hot spot residues identified in this investigation are conserved in the Bfr and Bfd sequences (Figure S11) of a large number of Gram-negative pathogens, where the *bfr* and *bfd* genes are also contiguous in the corresponding chromosomes (Table 3). Consequently, conservation in the arrangement of these genes in the chromosomes of many pathogens and conservation of hot spot residues in both proteins indicate that the hot region that stabilizes the BfrB:Bfd association in *P. aeruginosa* is likely to be of widespread significance in bacterial iron metabolism.

Table 3. Pathogens Where Adjacent *bfd* and *bfr* Genes Code Conserved Hot Spot Residues in the Corresponding Bfr and Bfd Sequences

	locus ID	
microorganism	*bfd*	*bfr*
Pseudomonas aeruginosa PAO1	PA3530	PA3531
Escherichia coli O157	Z4696	Z4695
Escherichia coli K12	b3337	b3336
Salmonella typhimurium	STM3444	STM3443
Salmonella enterica serovar Typhi	t4061	t4062
Salmonella enterica choleraesuis	SCH_3377	SCH_3378
Klebsiella pneumonia	KPN_03722	KPN_03723
Yersinia pestis	YPO0205	YPO0206
Yersinia pseudotuberculosis	YPTB3701	YPTB3700
Yersinia enterocolitica	YE3926	YE3925
Aeromonas salmonicida	ASA_0466	ASA_0467
Vibrio cholerae El	VC_0364	VC_0365
Vibrio cholerae	VC0395_A2775	VC0395_A2776
Vibrio vulnificus	VV1_1340	VV1_1341
Shigella flexneri 2a 2457T	S4406	S4407
Shigella flexneri 2a str301	AAN44819.1	AAN44818.1
Shigella dysenteriae	SDY_3499	SDY_3498
Erwinia carotovora	ECA4033	ECA4034
Enterobacter cloacae	ECL_04701	ECL_04700
Serratia sp.	SerAS12_4646	SerAS12_4645
Citrobacter koseri	CKO_04744	CKO_04743
Acinetobacter sp.	ACIAD3328	ACIAD3330

■ ASSOCIATED CONTENT

Supporting Information

The Supporting Information is available free of charge on the ACS Publications website at DOI: 10.1021/acs.biochem.5b00937.

Arsenic ion bound to the 4-fold pores of L^{68}A BfrB (Figure S1); Mg ion in the B-pore of L^{68}A BfrB (Figure S2); ITC and SPR analyses of the interaction between Bfd and M^0 BfrB (Figures S3 and S4); elution volumes of wt and mutant BfrBs from a calibrated size exclusion column (Figure S5); oxidized and reduced spectra of wt and mutant BfrBs (Figure S6); UV−vis spectra obtained from iron uptake of wt and mutant BfrBs (Figure S7); superposition of the ferroxidase centers of native and iron bound wt and L^{68}A/E^{81}A BfrB (Figure S8); UV−vis spectra of wt and mutant Bfds (Figure S9); overlay of double referenced sensorgrams resulting from injecting Bfd Y^2F and Bfd K^{40}A over immobilized BfrB (Figure S10); sequence alignment of *bfd* and *bfrb* genes from different pathogens (Figure S11); sequence of primer pairs used to introduce the sited-directed mutations; crystallographic data for wt and mutant BfrB structures (Table S1) (PDF).

Accession Codes

Coordinates and crystallographic structure factors for the distinct BfrB structures have been deposited in the Protein Data Bank under accession codes listed in Table S1 of the Supporting Information.

■ AUTHOR INFORMATION

Corresponding Author

*Telephone: 785-864-4936; Fax: 785-864-1916; E-mail: mrivera@ku.edu.

Funding

This study was supported by a grant from the National Science Foundation (M.R., MCB-1158469). A 2014 University of Kansas Strategic Grant, Level I, also supported this work.

Notes

The authors declare no competing financial interest.

■ ACKNOWLEDGMENTS

Use of the University of Kansas Protein Structure Laboratory was supported by grants from the National Center for Research Resources (5P20RR017708-10) and the National Institutes of General Medical Sciences (8 P20 GM 103420) from the National Institutes of Health. Use of the IMCA-CAT beamline 171D at the Advanced Photon Source was supported by the companies of the Industrial Macromolecular Crystallography Association through a contract with the Hauptman Wooward Medical Research Institute. Use of the Advanced Photon Source was supported by the U.S. Department of Energy, Office of Science, Office of Basic Energy Sciences, under contract no. DE-AC02-06CH11357. Dr. Na Zhang is acknowledged for performing preliminary exploratory SPR experiments.

DOI: 10.1021/acs.biochem.5b00937
Biochemistry 2015, 54, 6162−6175

REFERENCES

(1) Cornelis, P., Wei, Q., Andrews, S. C., and Vinckx, T. (2011) Iron homeostasis and management of oxidative stress response in bacteria. *Metallomics: integrated biometal science 3*, 540−549.

(2) Weinberg, E. D. (2009) Iron availability and infection. *Biochim. Biophys. Acta, Gen. Subj. 1790*, 600−605.

(3) Bullen, J. J., Rogers, H. J., Spalding, P. B., and Ward, C. G. (2005) Iron and Infection: The Heart of the Matter. *FEMS Immunol. Med. Microbiol. 43*, 325−330.

(4) Touati, D. (2000) Iron and oxidative stress in bacteria. *Arch. Biochem. Biophys. 373*, 1−6.

(5) Keyer, K., and Imlay, J. A. (1996) Superoxide accelerates DNA-damage by elevating free-iron levels. *Proc. Natl. Acad. Sci. U. S. A. 93*, 13635−13640.

(6) Honarmand Ebrahimi, K., Hagedoorn, P. L., and Hagen, W. R. (2015) Unity in the biochemistry of the iron-storage proteins ferritin and bacterioferritin. *Chem. Rev. 115*, 295−326.

(7) Rivera, M. (2014) Bacterioferritin: Structure Function and Protein−Protein Interactions, in *Handbook of Porphyrin Science* (Kadish, K. K., Smith, K. M., and Guilard, R., Eds.) pp 136−179, World Scientific, Hackensack, NJ.

(8) Andrews, S., Norton, I., Salunkhe, A. S., Goodluck, H., Aly, W. S., Mourad-Agha, H., and Cornelis, P. (2013) Control of iron metabolism in bacteria. *Met. Ions Life Sci. 12*, 203−239.

(9) Yao, H., Rui, H., Kumar, R., Eshelman, K., Lovell, S., Battaile, K. P., Im, W., and Rivera, M. (2015) Concerted motions networking pores and distant ferroxidase centers enable bacterioferritin function and iron traffic. *Biochemistry 54*, 1611−1627.

(10) Ruvinsky, A. M., Vakser, I. A., and Rivera, M. (2014) Local packing modulates diversity of iron pathways and cooperative behavior in eukaryotic and prokaryotic ferritins. *J. Chem. Phys. 140*, 115104.

(11) Andrews, S. C., Robinson, A. K., and Rodríguez-Quiñones, F. (2003) Bacterial iron homeostasis. *FEMS Microbiol. Rev. 27*, 215−237.

(12) Yao, H., Wang, Y., Lovell, S., Kumar, R., Ruvinsky, A. M., Battaile, K. P., Vakser, I. A., and Rivera, M. (2012) The structure of the BfrB-Bfd complex reveals protein-protein interactions enabling iron release from bacterioferritin. *J. Am. Chem. Soc. 134*, 13470−13481.

(13) Escolar, L., Perez-Martin, J., and De Lorenzo, V. (1999) Opening the Iron Box: Transcriptional Metalloregulation by the Fur Protein. *J. Bacteriol. 181*, 6223−6229.

(14) Vasil, M. L. (2007) How We Learnt About Iron Acquisition in *Pseudomonas aeruginosa*: A Series of Very Fortunate Events. *BioMetals 20*, 587−601.

(15) Oglesby-Sherrouse, A. G., and Murphy, E. R. (2013) Iron-responsive bacterial small RNAs: variations on a theme. *Metallomics: integrated biometal science 5*, 276−286.

(16) Masse, E., Vanderpool, C. K., and Gottesman, S. (2005) Effect of RyhB small RNA on global iron use in Escherichia coli. *J. Bacteriol. 187*, 6962−6971.

(17) Pandey, R., and Rodriguez, G. M. (2012) A ferritin mutant of *Mycobacterium tuberculosis* is highly susceptible to killing by antibiotics and is unable to establish a chronic infection in mice. *Infect. Immun. 80*, 3650−3659.

(18) Reddy, P. V., Puri, R. V., Khera, A., and Tyagi, A. K. (2012) Iron storage proteins are essential for the survival and pathogenesis of *Mycobacterium tuberculosis* in THP-1 macrophages and the guinea pig model of infection. *J. Bacteriol. 194*, 567−575.

(19) Chen, C. Y., and Morse, S. A. (1999) Neisseria gonorrhoeae bacterioferritin: structural heterogeneity, involvement in iron storage and protection against oxidative stress. *Microbiology 145*, 2967−2975.

(20) Expert, D., Boughammoura, A., and Franza, T. (2008) Sidreophore-Controlled Iron Assimilation in the Enterobacterium *Erwinia chrysanthemi*. *J. Biol. Chem. 283*, 36564−36572.

(21) Andrews, S. C., Harrison, P. M., and Guest, J. R. (1989) Cloning, Sequencing, and Mapping of the Bacterioferritin Gene (*bfr*) of *Escherichia coli* K-12. *J. Bacteriol. 171*, 3940−3947.

(22) Quail, M. A., Jordan, P., Grogan, J. M., Butt, J. N., Lutz, M., Thomson, A. J., Andrews, S. C., and Guest, J. R. (1996) Spectroscopic and Voltammetric Characterization of Bacterioferritin-Associated Ferredoxin of *Escherichia coli*. *Biochem. Biophys. Res. Commun. 229*, 635−642.

(23) Garg, R. P., Vargo, C. J., Cui, X., and Kurtz, D. M. J. (1996) A [2Fe-2S] Protein Encoded by an Open Reading Frame Upstream of the *Escherichia coli* Bacterioferritin Gene. *Biochemistry 35*, 6297−6301.

(24) Ochsner, U. A., Wilderman, P. J., Vasil, A. I., and Vasil, M. L. (2002) GeneChip Expression Analysis of the Iron Starvation Response in *Pseudomonas Aeruginosa*: Identification of Novel Pyoverdine Biosynthesis Genes. *Mol. Microbiol. 45*, 1277−1287.

(25) Palma, M., Worgall, S., and Quadri, L. E. N. (2003) Transcriptome Analysis of the *Pseudomonas aeruginosa* Response to Iron. *Arch. Microbiol. 180*, 374−379.

(26) Weeratunga, S., Gee, C. E., Lovell, S., Zeng, Y., Woodin, C. L., and Rivera, M. (2009) Binding of *Pseudomonas aeruginosa* Apobacterioferritin-Associated Ferredoxin to Bacterioferritin B Promotes Heme Mediation of Electron Delivery and Mobilization of Core Mineral Iron. *Biochemistry 48*, 7420−7431.

(27) Weeratunga, S., Lovell, S., Yao, H., Battaile, K. P., Fischer, C. J., Gee, C. E., and Rivera, M. (2010) Structural Studies of Bacterioferritin B (BfrB) from *Pseudomonas aeruginosa* Suggest a Gating Mechanism for Iron Uptake via the Ferroxidase Center. *Biochemistry 49*, 1160−1175.

(28) Wang, A., Zeng, Y., Han, H., Weeratunga, S., Morgan, B. N., Moenne-Loccoz, P., Schonbrunn, E., and Rivera, M. (2007) Biochemical and structural characterization of *Pseudomonas* aeruginosa Bfd and FPR: ferredoxin NADP+ reductase and not ferredoxin is the redox partner of heme oxygenase under iron-starvation conditions. *Biochemistry 46*, 12198−12211.

(29) Wong, S. G., Abdulqadir, R., Le Brun, N. E., Moore, G. R., and Mauk, A. G. (2012) Fe-haem bound to *Escherichia coli* bacterioferritin accelerates iron core formation by an electron transfer mechanism. *Biochem. J. 444*, 553−560.

(30) Berry, E. A., and Trumpower, B. L. (1987) Simultaneous determination of hemes a, b, and c from pyridine hemochrome spectra. *Anal. Biochem. 161*, 1−15.

(31) Ringeling, P. L., Davy, S. L., Monkara, F. A., Hunt, C., Dickson, D. P., McEwan, A. G., and Moore, G. R. (1994) Iron metabolism in *Rhodobacter capsulatus*. Characterisation of bacterioferritin and formation of non-haem iron particles in intact cells. *Eur. J. Biochem. 223*, 847−855.

(32) Kabsch, W. (2010) Integration, scaling, space-group assignment and post-refinement. *Acta Crystallogr., Sect. D: Biol. Crystallogr. 66*, 133−144.

(33) Evans, P. R. (2011) An introduction to data reduction: space-group determination, scaling and intensity statistics. *Acta Crystallogr., Sect. D: Biol. Crystallogr. 67*, 282−292.

(34) McCoy, A. J., Grosse-Kunstleve, R. W., Adams, P. D., Winn, M. D., Storoni, L. C., and Read, R. J. (2007) *Phaser* crystallographic software. *J. Appl. Crystallogr. 40*, 658−674.

(35) Adams, P. D., Afonine, P. V., Bunkoczi, G., Chen, V. B., Davis, I. W., Echols, N., Headd, J. J., Hung, L. W., Kapral, G. J., Grosse-Kunstleve, R. W., McCoy, A. J., Moriarty, N. W., Oeffner, R., Read, R. J., Richardson, D. C., Richardson, J. S., Terwilliger, T. C., and Zwart, P. H. (2010) PHENIX: a comprehensive Python-based system for macromolecular structure solution. *Acta Crystallogr., Sect. D: Biol. Crystallogr. 66*, 213−221.

(36) Emsley, P., Lohkamp, B., Scott, W. G., and Cowtan, K. (2010) Features and development of Coot. *Acta Crystallogr., Sect. D: Biol. Crystallogr. 66*, 486−501.

(37) Chen, V. B., Arendall, W. B., 3rd, Headd, J. J., Keedy, D. A., Immormino, R. M., Kapral, G. J., Murray, L. W., Richardson, J. S., and Richardson, D. C. (2010) MolProbity: all-atom structure validation for macromolecular crystallography. *Acta Crystallogr., Sect. D: Biol. Crystallogr. 66*, 12−21.

(38) Matthews, B. W. (1968) Solvent content of protein crystals. *J. Mol. Biol. 33*, 491−497.

(39) Qiu, F., Rivera, M., and Stark, R. E. (1998) An ^{1}H-^{13}C-^{13}C-Edited ^{1}H NMR Experiment for Making Resonance Assignments in the Active Site of Heme Proteins. *J. Magn. Reson. 130*, 76−81.

DOI: 10.1021/acs.biochem.5b00937
Biochemistry 2015, 54, 6162−6175

(40) Wilkinson, K. D. (2004) Quantitative analysis of protein-protein interactions. *Methods Mol. Biol. 261*, 15−32.
(41) Morton, T. A., and Myszka, D. G. (1998) Kinetic analysis of macromolecular interactions using surface plasmon resonance biosensors. *Methods Enzymol. 295*, 268−294.
(42) Biacore. (2012) Analysis of kinetics and concentration measurements, in Appendix A, *Biacore Assay Handbook*, GE Healthcare Life Sciences.
(43) Krissinel, E. (2012) Enhanced fold recognition using efficient short fragment clustering. *J. Mol. Biochem. 1*, 76−85.
(44) Krissinel, E., and Henrick, K. (2004) Secondary-Structure Matching (SSM), A New Tool for Fast Protein Structure Alignment in Three Dimensions. *Acta Crystallogr., Sect. D: Biol. Crystallogr. 60*, 2256−2268.
(45) Clackson, T., and Wells, J. A. (1995) A hot spot of binding energy in a hormone-receptor interface. *Science 267*, 383−386.
(46) Bogan, A. A., and Thorn, K. S. (1998) Anatomy of hot spots in protein interfaces. *J. Mol. Biol. 280*, 1−9.
(47) Keskin, O., Gursoy, A., Ma, B., and Nussinov, R. (2008) Principles of protein-protein interactions: what are the preferred ways for proteins to interact? *Chem. Rev. 108*, 1225−1244.
(48) Keskin, O., Ma, B., and Nussinov, R. (2005) Hot regions in protein–protein interactions: the organization and contribution of structurally conserved hot spot residues. *J. Mol. Biol. 345*, 1281−1294.

DOI: 10.1021/acs.biochem.5b00937
Biochemistry 2015, 54, 6162−6175